frontiers | Frontiers in Catalysis

TYPE Original Research
PUBLISHED 04 August 2022
DOI 10.3389/fctls.2022.890842

OPEN ACCESS

EDITED BY
Nathan Skillen,
The University of Manchester,
United Kingdom

REVIEWED BY
Sanjay Nagarajan,
University of South Wales,
United Kingdom
Jingxiang Low,
University of Science and Technology of China, China

*CORRESPONDENCE
Jenny Schneider,
jenny.schneider@lmu.de

SPECIALTY SECTION
This article was submitted to Photocatalysis, a section of the journal Frontiers in Catalysis

RECEIVED 06 March 2022
ACCEPTED 01 July 2022
PUBLISHED 04 August 2022

CITATION
Hailili R, Bahnemann DW and Schneider J (2022), Ionic liquid-mediated microstructure regulations of layered perovskite for enhanced visible light photocatalytic activity.
Front. Catal. 2:890842.
doi: 10.3389/fctls.2022.890842

Ionic liquid-mediated microstructure regulations of layered perovskite for enhanced visible light photocatalytic activity

Reshalaiti Hailili[1,2,3], Detlef W. Bahnemann[1,4] and Jenny Schneider[2]*

[1]Institut für Technische Chemie, Gottfried Wilhelm Leibniz Universität Hannover, Hannover, Germany, [2]Department of Chemistry, Ludwig-Maximilians-Universität (LMU) München, München, Germany, [3]MOE Key Laboratory of Enhanced Heat Transfer and Energy Conservation, Beijing Key Laboratory of Heat Transfer and Energy Conversion, Beijing University of Technology, Beijing, China, [4]Laboratory "Photoactive Nanocomposite Materials", Saint Petersburg State University, Saint-Petersburg, Russia

The presence of pollutants, e.g., pharmaceutical residues and industrial pollutants causes serious risks and irreversible damage to public health and ecological balance. Semiconductor-based photocatalysis is an attractive way to treat polluted water. Rational design and nanostructuring of semiconductors with visible light absorption and prominent surfaces could strengthen surface-interface reactions, resulting in improved photocatalytic degradation. Herein, layered structured perovskites $Bi_4Ti_3O_{12}$ (BTO) were synthesized by an ionic liquid [1-butyl-3-methylimidazolium iodide (Bmim)I] assisted approach. The precise tuning of synthetic conditions allowed formations of various microstructures, including spherical nanoparticles, nanoplates and nanorods, respectively. The optical analyses demonstrated that samples were typically visible light absorbents with narrow band gap energies (2.96–2.73 eV), and displayed pronounced degradation for pharmaceutical residues under visible light illumination. The factors responsible for the high efficiency of BTO photocatalysts were discussed in terms of unique structure, optical alignment, dipole induced carrier separation and formation of active radicals. Among studied samples, the nanorod shaped BTO showed 1.31 and 1.46 times higher apparent rate constants for tetracycline and ibuprofen degradation than its counterparts (spherical nanoparticles and nanoplates), respectively. The better performance of nanorods was ascribed to their higher visible light harvesting ability. Importantly, BTO nanorods exhibited nonselective degradation activity for diverse pollutants of pharmaceutical residues and industrial contaminants. This work demonstrates the unique strategy of microstructure regulation and a wide range of applications of layered perovskites for environmental remediation.

KEYWORDS

microstructure, layered perovskite, ionic liquid, photocatalysis, environmental remediation

Introduction

Widely consumed pharmaceutics have been used in the pharmaceutical industry and enter the environment in large amounts (Keen and Linden, 2013). Existing pharmaceutical residues and industrial pollutants present in water and food have hidden risks to human health and the ecosystem. (Hoffmann et al., 1995; Rappaport and Smith, 2010). Hence, removal of such contaminants is required. Solar-light-driven photocatalysis has been considered as the frontier method to treat pollutants. Many successful state-of-the-art photocatalysts have been developed for contaminant treatments, e.g., the famous "star" photocatalyst TiO_2 (Fujishima and Honda, 1972; Gong et al., 2021) and sulfides (Zong et al., 2008). However, reaction yields of the oxides remain low under visible light illumination, while sulfides suffer from low photostability. Efforts have been devoted to the efficiency enhancement of the photocatalysts by regulating their microstructure e.g., crystal facets (Li et al., 2013), morphology (Chen et al., 2010), band gap energy (Schneider et al., 2014; Wei et al., 2020) and surface defects (Gao et al., 2017). Rational design and microstructure regulations of photocatalysts could improve charge carrier separation and enhance light harvesting efficiency.

Bismuth titanates-based photocatalysts such as $Bi_4Ti_3O_{12}$ (Liu et al., 2020; Wang et al., 2022), $Bi_{20}TiO_{32}$ (Hou et al., 2013) and $Bi_{12}TiO_{20}$ (Zhu et al., 2011) have been attracting wide attention due to their appealing electronic band structure, high stability and "earth-abundant" nature. $Bi_4Ti_3O_{12}$ (BTO) is one of the most important layered Bi, Ti-based photocatalysts investigated for various environmental applications. (Yao et al., 2004; Zhang et al., 2009). The layered-structured materials, especially Bi-based layered perovskites, (Hailili et al., 2022; Lv et al., 2022), have raised significant interest as a photocatalyst mainly due to the following beneficial features: 1) The BTO acquires a typical Aurivillius-type layered structure that is alternatively arranged with triple layers of $[Bi_2Ti_3O_{10}]^{2-}$ sandwich and a fluorine-like $[Bi_2O_2]^{2+}$ layers along the *c* axis direction; in such crystal structures the dipole effects and built-in-electric field occur upon variation of the illumination which is beneficial to the charge carrier transport; 2) the positively charged $[Bi_2O_2]^{2+}$ layers and negatively charged counter slabs can endow internal static electronic field for the effective directional charge carrier separation; 3) the layered-structured materials are highly tunable and thus diverse microstructures and surface-interfaces can be created enabling the control of the diffusion distance and density of the photogenerated charge carriers; 4) surface-interface control (e.g., crystal facets, morphology, surface defects); in the layered photocatalysts was anticipated to optimize the photocatalytic process through the adjustment of the surface interactions which influence the probe molecule adsorption mode and thus the reaction pathway upon light illumination. Generally, BTO applied for pollutant degradation was synthesized at high temperatures of 400–1000°C by a solid-state method (Yao et al., 2003). Unfortunately, the activity of BTO remains low due to its undesirable microstructure, which results from the synthetic methods. It is demanding to prepare well-microstructured BTO particles by means of the more moderate and green synthetic methods rather than through traditional tedious solid-state reactions.

A new solvent system, ionic liquids, attracts broad interest for the inorganic crystals synthesis due to their intrinsically ionic characteristics, negligible vapor pressure, good dissolving ability, thermal stability and high ionic conductivity (Ren et al., 2020; Zhang et al., 2020). The physicochemical properties of the ionic liquids are easily tunable thanks to their designable structure thus they can serve as environmentally benign solvents for microstructure regulations (Zhang et al., 2020). For instance, TiO_2 nanocuboids with active {100} and {001} facets were obtained using acetic acid and 1-butyl-3-methylimidazolium tetrafluoroborate ([Bmim][BF_4]) instead of introducing HF (Zhao et al., 2011). Employing [Bmim]I as a surface-modified agent, BiOI nanoplates were prepared for photocatalytic pollutant degradation (Wang et al., 2011). Morphological design of $Bi_{12}TiO_{20}$ was achieved in the presence of [Bmim]Br which displayed enhanced photocatalytic activity (Ren et al., 2016). Hence, replacing a solvent with ionic liquids can lead to the remarkable control over the microstructural properties of nanomaterials.

Considering the advantages of the ionic liquid for material synthesis, an ionic liquid 1-butyl-3-methylimidazolium iodide ([Bmim]I) was incorporated into the synthesis of BTO photocatalysts. With an ionic-liquid assistant method, remarkable control of the microstructure and optical response (up to 2.73 eV) of BTO were achieved merely through the adding volume of [Bmim]I. As-obtained BTO served as the visible active photocatalyst for the environmental remediation of the pharmaceutical residues and industrial pollutants. The structure-property relationship of BTO was discussed in terms of microstructure, crystal structure and optical properties.

Materials and methods

Chemicals

All chemicals used in our experiment were of analytical grade and used without further purification. The employed raw materials were purchased from Shanghai Aladdin Bio-Chem Technology Co., Ltd. (Shanghai, China). Employed aqueous solutions were prepared using ultrapure (deionized) water. The target BTO photocatalysts were synthesized by an ionic-liquid assisted one-step hydrothermal method using 1-butyl-3-methylimidazolium iodide ([Bmim]I) as solvent.

Synthesis of ionic liquid

[Bmim]I was prepared according to the literature procedure (Huddleston et al., 2001). A mixture of equal molar amounts of iodobutane (0.40 mol) and 1-methylimidazole (0.40 mol) were added to a flask followed by vigorous stirring and underwent oil bath heating at 70–80°C for 48 h. After the reaction, two uniform phases were observed, the top containing unreacted raw materials. The further treatment was washing and cleaning by mixing with ethyl acetate. These procedures were repeated several times, each time fresh ethyl acetate was added to remove any residual material from the bottom phase to acquire a pure product. Further heating at 70°C was performed to remove any remaining ethyl acetate. Finally, the product was stirred under a vacuum and cooled to room temperature. A slightly darker product, [Bmim]I, was obtained (~ yields of about 92%).

Preparation of photocatalysts

The BTO samples were synthesized by an ionic liquid assisted hydrothermal approach. In a typical procedure, bismuth nitrate pentahydrate [$Bi(NO_3)_3{\cdot}5H_2O$, 3.29 mmoL] and sodium hydroxide (NaOH, 0.1 moL) were added to 30 ml distilled water and stirred for 40 min to obtain a highly soluble and homogeneous precursor solution. Upon stirring, tetrabutyl titanate [$Ti(OC_4H_9)_4$, 2.4 mmoL] was slowly dropped into the above solution. After continuous stirring for 30 min at room temperature, self-synthesized ionic liquid [Bmim]I (0.5, 2.0 and 3.0 ml) was carefully added to the above solution followed by continuous stirring for 40 min to gain a well-uniformed solution. At the end of the synthesis, the prepared mixture was poured into a Teflon autoclave and heated at 150°C for 18 h. After that, samples were cooled to room temperature, filtered and washed with the mixture of distilled water and absolute ethanol several times, and dried at 60°C in an oven overnight. For accuracy, the samples obtained in [Bmim]I was labeled as BTO–S (0.5 ml), BTO–P (2.0 ml), and BTO–R (3.0 ml), respectively.

Characterization

The scanning electron microscopy images (SEM) were observed on a Hitachi S-3500N SEM. The transmission electron microscopy (TEM) and High-resolution TEM (HRTEM) characterization were performed on a JEOL-JEM 2100 electron microscope. The Brunauer–Emmett–Teller (BET) surface areas were quantified by means of a Quantachrome Instrument (QUADRASORB IQ). Before the measurements, 50.0 mg of the sample were degassed at 180°C for 3 h. X-ray powder diffraction of the samples was measured at room temperature in the angular range of 3–80° with a scan step width of 0.06°/s and on a Bruker D8 ADVANCE X-ray diffractometer equipped with graphite monochromatized Cu Kα radiation (λ = 0.154 nm). The crystal structure simulations were performed *via POWDERCELL* and *Mercury 3.0.17* software and further analyzed to obtain crystal structure. A Fourier Transform Infrared Spectra (FTIR) of the samples were recorded at room temperature with KBr pellets containing ca. 1.0 mg of the sample. Spectra were recorded in the wavenumber range from 400 cm^{-1} to 4000 cm^{-1} with a resolution of 2 cm^{-1} using Bruker Optics TENSOR 27 FTIR. UV-vis diffuse-reflectance spectra (DRS) of 25.0 mg of a sample mixed with $BaSO_4$ were recorded in the wavelength range from 200 to 800 nm using an UV-vis spectrophotometer (UV-3700, Shimadzu, Japan).

Photocatalytic activity tests

The photocatalytic activity of the prepared samples was evaluated by decomposing pharmaceutical residues, such as tetracycline and ibuprofen, and by decomposing dyes such as Rhodamine B (RhB) and Methyl orange (MO) at ambient temperature. The specially designed 150 ml quartz beaker was used as the main reactor, above which a 300 W Xe lamp (cut-off filter ≥420 nm, PLS-SXE300, Perfect Light Company, Beijing, China) was arranged as the light source. The light intensity was 300 mW cm^{-2}. In the experiment, 45.0 mg of as-obtained BTO photocatalyst were dispersed in 100.0 ml an aqueous solution containing the pollutant concentration of 5.0×10^{-4} moL L^{-1}. The obtained suspension was stirred in the dark for 40 min with a speed of 400 r mim^{-1}, the time required to achieve the adsorption-desorption equilibrium and uniform distribution of the photocatalyst and pollutants. After that, the reaction mixture was exposed to light illumination. After a given illumination time and 3 min of sedimentation, two separate phases of photocatalyst powder and the aqueous transparent solution were obtained. Following this procedure, about 10.0 ml of the solution was withdrawn from the top phase, and the photocatalyst was further separated from the suspensions by quick centrifugation with 10,000 r mim^{-1} for 10 min. The concentration changes of the pollutant in the course of the illumination time were monitored through a wavelength scan by means of a UV-3700 spectrophotometer at the wavelengths of 355.5 nm (for tetracycline), 262.0 nm (for ibuprofen), 549 nm (for RhB), and 462 nm (for MO), respectively. More precise detection of the change in pollutant concentration was achieved by separation methods, which were performed on high performance liquid chromatography (HPLC, UltiMate 3000, United States) with a VWD detector using a Cosmosil 5C18-MS-II (particle size 5.0 mm, 4.6 × 250 mm). To examine the recyclability of BTO photocatalyst, samples in the centrifugal tube and beaker were collected and combined together, then were subsequently immersed into the fresh pollutant-containing solution. The above procedure was performed for multi-cycles to evaluate the long-term suitability of the BTO samples.

Total organic carbon measurements

The mineralization degree of as-selected pollutants was analyzed by TOC tests. Typically, the final decomposition products of pollutants were filtered with a 0.45 μm filter and further tested on a vario TOC (Elementar, Germany) analyzer. A standard potassium hydrogen phthalate solution was applied for the standard curve fitting, and the corresponding TOC was estimated from the following equation (Tong et al., 2012):

$$\text{TOC removal } (\%) = \frac{\text{TOC}_o - \text{TOC}_t}{\text{TOC}_o} \times 100\%$$

where TOC_o is an initial TOC, and TOC_t is a varied TOC at a given time t in ppm.

Electron spin resonance measurements

To clarify the role of the photogenerated radicals such as superoxide radicals ($O_2^{\cdot-}$) and hydroxyl radicals ($^{\cdot}OH$) in the photocatalytic reaction, a spin trapping agent 5, 5-dimethyl-1-pyrroline N-oxide (DMPO) was applied. In a typical procedure, 8.5 mg of the photocatalyst were dispersed in 2.40 ml of methanol/water mixture, which was bubbled with oxygen for 30 min, and then was vigorously shaken for 30 s followed by the addition of 25.0 μl DMPO solution. The obtained mixture was analyzed by EPR-Spectroscopy after being irradiated with a 300 W Xe lamp (with 420 nm cut-off filter) for a given time interval.

Radical trapping tests

Following scavengers were added to the photocatalyst pollutant-suspension to determine the contributions of photogenerated active radicals formed during the photocatalytic degradation processes: 3.5 mmoL isopropanol (IPA): $^{\cdot}OH$-radicals, 3.5 mmoL *p*-benzoquinone (PBQ): $O_2^{\cdot-}$ radicals, 3.5 mmoL ammonium oxalate (AO): h^+ and 3.5 mmoL potassium dichromate ($K_2Cr_2O_7$): e^-. In addition, the experiments were also performed in N_2 atmosphere to identify the role of oxygen in the system. The radical trapping tests were performed under similar conditions as the degradation tests except for the addition of the corresponding scavenger to the reaction.

Results and Discussion

Structural and morphological characterization

Figure 1A presents the XRD patterns of BTO-S (0.5 ml of [Bmim]I), BTO-P (2.0 ml of [Bmim]I), and BTO-R (3.0 ml of [Bmim]I) samples synthesized by an ionic liquid assisted hydrothermal method, respectively. All patterns could be indexed as the standard phase of BTO (JCPDS Card No. 35–0795), which crystallizes in an orthorhombic space group with the lattice parameters being a = 5.41 Å, b = 5.448 Å, c = 32.84 Å, respectively. No characteristic peaks of any impurities from unreacted reactants or added ionic liquids were detected, confirming high phase purity. Hence, with a moderate preparation procedure, highly crystalline BTO can be obtained merely by adjusting the adding volume of [Bmim]I during the synthesis.

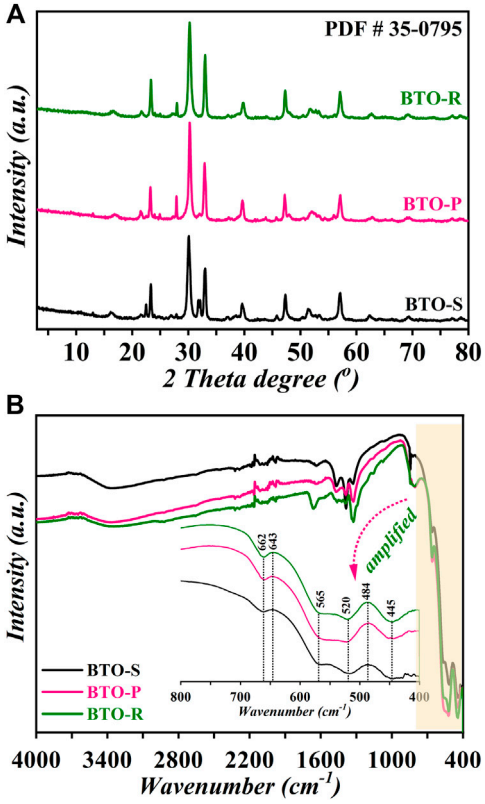

FIGURE 1
(A) XRD patterns and **(B)** FTIR spectra of BTO photocatalysts synthesized in the presence of different [Bmim]I volume (black) BTO-S (0.5 ml); (pink) BTO-P (2.0 ml); (green) BTO-R (3.0 ml).

FTIR-spectra were recorded to characterize the surface chemistry of BTO photocatalysts. Figure 1B shows the FTIR bands of the BTO constituents. As displayed in the amplified vibration spectra, the bands at 445, 484, 520, 565, 643 and 662 cm^{-1} were assigned to the Bi–O and Ti–O vibration modes of BTO nanocrystals, respectively (Liu et al., 2021). The vibrations at 445, 662 cm^{-1}, and in the wavenumber range between 520 and 565 cm^{-1} recorded for BTO–P and BTO–R samples are stronger than the same vibrations for that of BTO–S, indicating the structural variations associated with Ti–O and Bi–O bonds, respectively. Furthermore, no

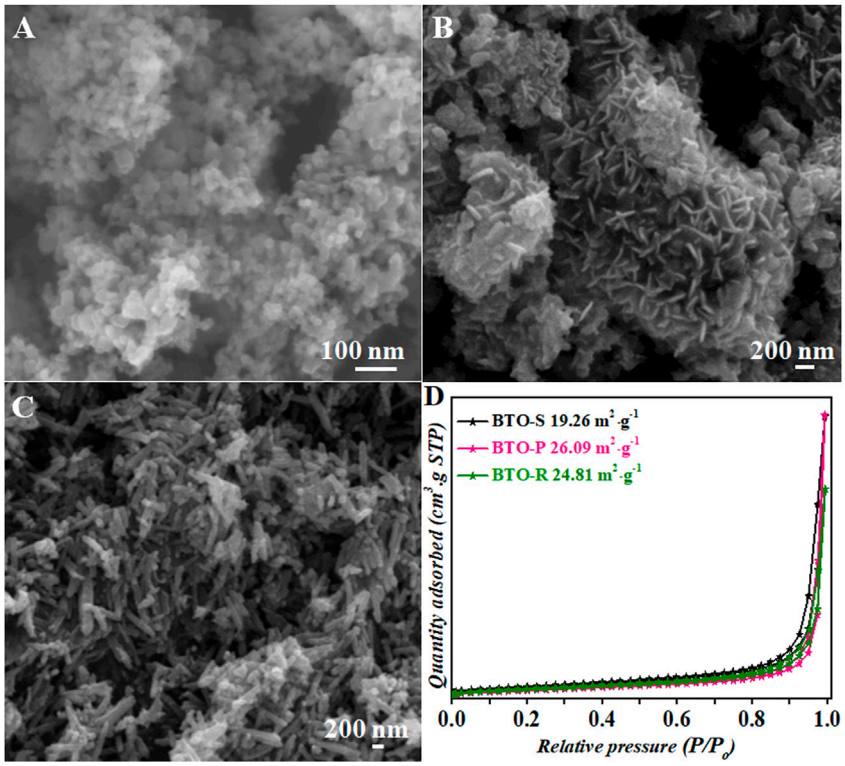

FIGURE 2
SEM images of BTO photocatalysts synthesized in the presence of different [Bmim]I volume: **(A)** BTO-S (0.5 ml); **(B)** BTO-P (2.0 ml); **(C)** BTO-R (3.0 ml). **(D)** Nitrogen adsorption–desorption isotherms of BTO photocatalysts, respectively.

apparent bands from the introduced ionic liquid appeared in the whole spectral region.

The various microstructures of BTO samples obtained in the presence of different volumes of ionic liquid are demonstrated by SEM images (Figure 2). When BTO is prepared with the assistance of 0.5 ml [Bmim]I, the as-obtained BTO–S is comprised of very uniform spherical nanoparticles with an average size of 20–40 nm and 98% product yield (Figure 2A). Herein, with the addition of the trace amount of the ionic liquid, the main driving force for the nucleation might become higher due to the low interface tensions of [Bmim]I. Meanwhile, the nucleation rates get enhanced influencing the self-organization of BTO and as a result, spherical nanoparticles are formed. Interestingly, with the addition of 1.0 ml [Bmim]I to the synthesis, the morphology of BTO was rapidly changed to the nanoplates with a thickness of about 20–30 nm (Supplementary Figure S1, in the supporting information, SI). However, when the adding volume of [Bmim]I was further increased to 2.0 ml, the microstructure of BTO appeared as uniform assembled nanoplates (BTO–P). Careful examination of the morphology reveals that many tortilla nanoplates arrange themselves in an intersection-centric manner (Figure 2B). We conclude from these observations that $[Bmim]^+$ in the reaction acts as a structure-directing agent and facilitates the anisotropic growth leading to assorted microstructures. Such curtail roles of solvents on the microstructure regulations were reported (Zhang et al., 2021). The formation of nanoplate structures might also be related to a layered crystal structure of BTO composed of $[Bi_2O_2]^{2+}$ slices and TiO_6 octahedral layers. Similar formation of plate-like nanostructures was reported for [Bmim]I modified BiOI (IL–BiOI) (Wang et al., 2011). The addition of 3.0 ml [Bmim]I to the reaction mixture causes significant structural changes and initiates the formation of uniformly dispersed nanorods BTO–R, with an average length of 400–800 nm and diameter of 20–40 nm, respectively (Figure 2C). It is worth mentioning that the synthesis performed in the absence of [Bmim]I yielded particles with irregular shapes and low crystallinity (Supplementary Figure S2, in the SI). This observation confirms the role of [Bmim]I in the system as both solvent and structure-directing agent, which is favorable for the directional growth of BTO crystal and the formation of ordered microstructures.

The surface areas of BTO photocatalysts were quantified to be 19.26 g^{-1} m^2 (BTO–S), 26.09 g^{-1} m^2 (BTO–P) and 24.81 g^{-1} m^2 (BTO–R), respectively (Figure 2D). Among the samples, BTO–P possesses the largest surface area, which is

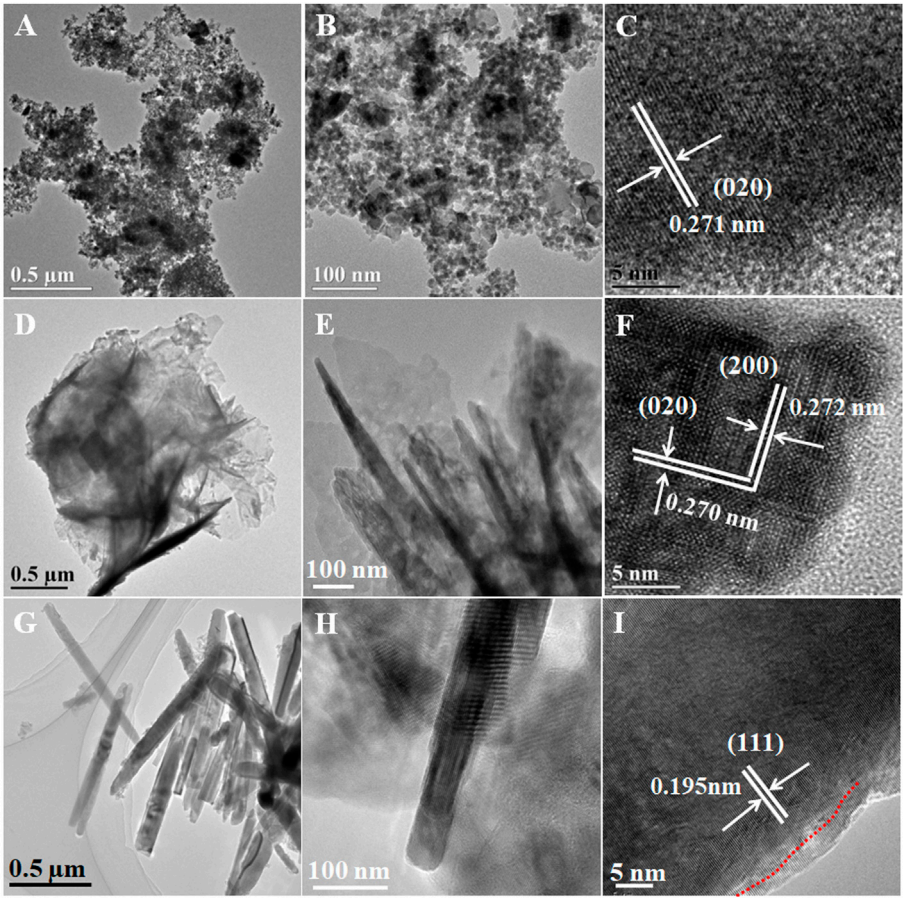

FIGURE 3
TEM/HRTEM images of BTO photocatalysts synthesized in the presence of different [Bmim]I volume: **(A–C)** BTO-S (0.5 ml); **(D–F)** BTO-P (2.0 ml); **(G–I)** BTO-R (3.0 ml).

16.3 folds and 2.45 times larger than the reported BET areas of sol-gel and hydrothermally synthesized BTO nanoplates (1.6 g^{-1} m^2 and 10.6 g^{-1} m^2), respectively (Liu et al., 2020). The relatively high surface areas of BTO samples should possess more catalytic active sites and thus be beneficial for the adsorption and degradation of target pollutants.

TEM/HRTEM characterization allows a deeper structural analysis of the BTO samples (Figure 3). Uniformly alighted spherical nanoparticles were recorded for BTO–S (Figures 3A,B), consistent with the obtained results of their SEM profiles. A unique lattice spacing of two lattice fringes was measured to be 0.271 nm, which is assigned to the (020) crystal plane (Figure 3C). The nanoplates in BTO–P were stacked together and exhibited thick petals (Figures 3D,E). The edges of those gathered nanoplates were analyzed and two sets of unique lattices spacing with the average spacing of 0.272 and 0.270 nm were quantified, which were assigned to the (200) and (020) planes of BTO crystal (Figure 3F). These results evince that in-plane surfaces of the BTO–P lie in (001) facets. The lattice structure of one single nanorod of BTO-R was analyzed (Figures 3G,H), in which the interlayer distances were determined to be 0.195 nm, indicating the (111) planes of BTO (Figure 3I). This suggests that in the presence of the higher [Bmim]I amount BTO grows seamlessly along {01-1} direction to yield nanorods validating the significant role of ionic liquid during the BTO formation.

From the presented morphological and structural characterization, we can conclude that in the case of BTO–P $[Bmin]^+$ from the ionic liquid acts as the capping agent, which selectively adsorbs on the specific surfaces and stabilizes, or even selectively etching facets such as (001), further reducing the energy to form the captured plates of BTO–P. Upon increase of [Bmim]I amount, the side-by-side assembly of the nanoplates is hindered in a certain direction and preferential growth takes place due to an entropy-driven process. From the structural point of view, the hydrogen atoms from the imidazolum ring of ionic liquid would construct a weak bond with oxygen atoms from $[Bi_2O_2]^{2+}$ layers on the (111) plane, leading to directional

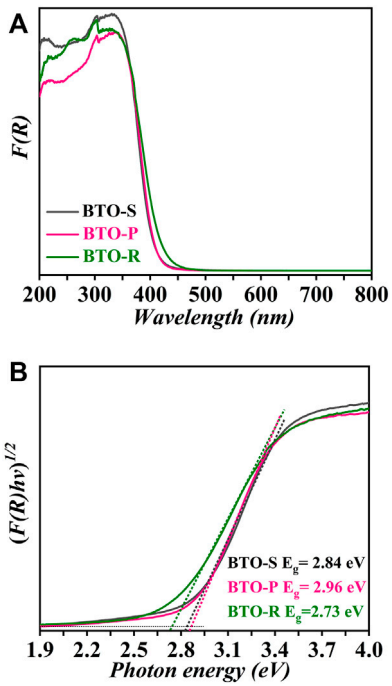

FIGURE 4
(A) Diffuse reflectance spectra and **(B)** Tauc plots of the modified Kubelka-Munk function of BTO photocatalysts synthesized in the presence of different [Bmim]I volume (black) BTO-S (0.5 ml); (pink) BTO-P (2.0 ml); (green) BTO-R (3.0 ml).

alignments and resulting in observed nanorods of BTO–R. Hence, the growth process of BTO is directly influenced by the adding amount of [Bmim]I and leads to the diverse structures of well-defined morphology.

Optical characterization

The optical properties of three BTO photocatalysts were investigated by means of UV-vis diffuse reflectance spectroscopy (DRS). The measured reflectance was converted into the Kubelka-Munk function according to the following equations: (Kubelka and Munk, 1931; Nobbs, 1985):

$$F(R_\infty) = (1 - R_\infty)^2 / 2R_\infty = \alpha/S \quad (1)$$

$$R_\infty = R_{catal.}/S_{BaSO4} \quad (2)$$

where F (R_∞), R, α and S are the Kubelka-Munk function, reflectance, absorption coefficient and scattering coefficient, respectively. The corresponding F(R) spectra are shown in Figure 4A. All samples exhibit strong light absorption below 460 nm. The corresponding absorption edges shift towards longer wavelengths in the order BTO-P, BTO-S and BTO-R. The band gap energies of the three samples were quantified by evaluation of the Tauc plots, herein an indirect optical transition was assumed. (Kubelka and Munk, 1931; Tauc, 1968; Nobbs, 1985):

$$(\alpha h\nu)^n = \left(h\nu - E_g\right) \quad (3)$$

where hν is discrete photon energy and α is the absorption coefficient of the material, n is related to the type of the optical transition. Here it was assumed $\alpha = F(R)$ and $n = 1/2$ for indirect transition. The graphs of $[F(R)h\nu]^{1/2}$ vs. (hν) for all samples are plotted in Figure 4B. By extrapolating the linear portion of $[F(R)h\nu]^{1/2}$ vs. (hν) to F(R) = 0, the E_g values for the BTO samples were obtained. The band gap energies are found to be 2.84 eV (BTO–S), 2.96 eV (BTO–P), and 2.73 eV (BTO–R), respectively. All estimated band gap energies are lower than reported values of 3.08–3.22 eV (Yao et al., 2004; Zhang et al., 2009; Liu et al., 2020; Wang et al., 2022).

To the best of our knowledge, we report for the first time the dependency of the band gap energy on the microstructure of the BTO photocatalysts. Normally such dependencies are demonstrated for quantum-sized semiconductors, however, in the present case the BTO nanoparticles are too large to exhibit this effect. The XPS analysis (Supplementary Figure S3, in the SI) revealed that the amounts of the oxygen defects do not differ significantly between the three BTO samples. We think that the structure dependent E_g might be related to the instinct crystal structure of BTO, which would display a certain polarization with external driving forces. This is very similar to the case of BiOCl, which also shows E_g changes originated from light-induced surface defects. (Wu et al., 2017).

The structural, morphological, and optical properties are known to influence the photocatalytic performance of the photocatalysts. The corresponding properties of the three BTO photocatalysts are summarized in Table 1. For better comparison of the light harvesting ability of BTO photocatalysts the F(R), integrated over the wavelength range, which is applied in photocatalytic tests, namely from 420 to 800 nm, is reported.

Photocatalytic performance

The environmental implementations of the synthesized BTO photocatalysts were studied by decomposing the pharmaceutical residues such as tetracycline and ibuprofen under illumination with 300 W Xe lamp (cut-off filter ≥420 nm, light intensity of 300 mW cm^{-2}). Figures 5A,C show concentration changes of tetracycline and ibuprofen as reaction time increases. The corresponding concentration changes (C/C_0, %) of the studied pollutants were quantified by means of the empirical equation $[(C_o - C_t)/C_o] \times 100\%$, where C_o and C_t are the concentrations of the pollutants at t = 0 and after given irradiation time t (Minero et al., 2013). In the absence of the photocatalyst or light, no or negligible concentration changes of the studied pollutants were

TABLE 1 The structural, morphological, and optical properties of the three BTO photocatalysts.

Photocatalysts	[Bmin]I (ml)	Shape	E_g (eV)	BET (g^{-1} m^2)	F(R) (420–800 nm)
BTO–S	0.5	Nanospheres	2.84	19.26	1.1562
BTO–P	2.0	Nanoplates	2.96	26.09	0.8062
BTO–R	3.0	Nanorods	2.73	24.81	2.4191

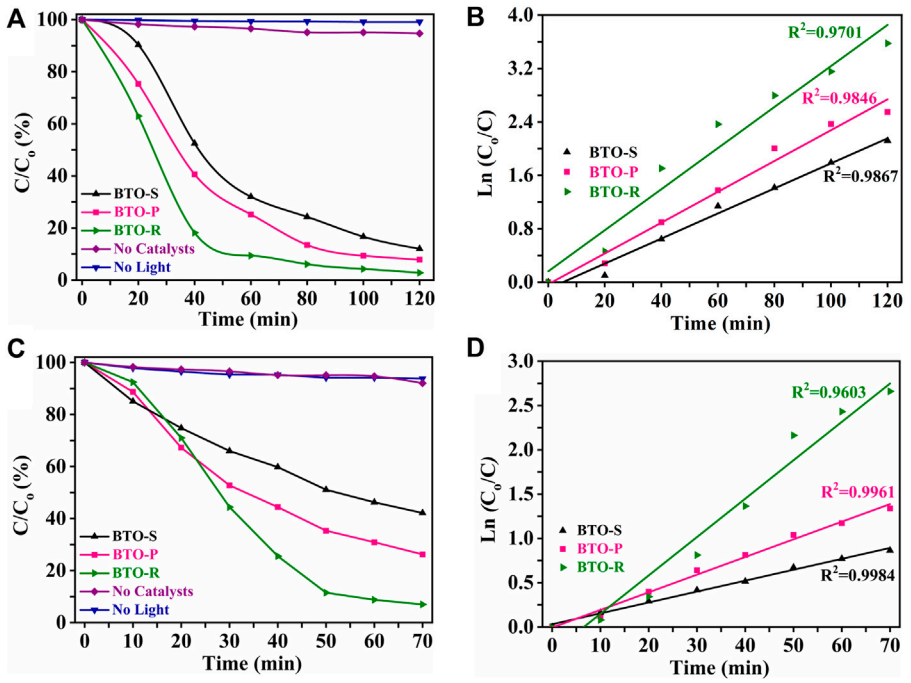

FIGURE 5
(A,C) Visible-light-driven tetracycline and ibuprofen degradation using BTO photocatalysts synthesized in the presence of different [Bmim]I volume (black) BTO-S (0.5 ml); (pink) BTO-P (2.0 ml); (green) BTO-R (3.0 ml). **(B,D)** The first-order reaction kinetics and corresponding regression coefficient (R^2) for tetracycline and ibuprofen decompositions, respectively.

detected, indicating that the decomposition process requires both photocatalyst and light exposure. All three BTO samples are suitable to decompose tetracycline and ibuprofen upon visible light illumination. However, the photocatalytic activity depends on the applied BTO photocatalyst. Hence, the residential concentration of tetracycline after 120 min visible light illumination follows the order: BTO–R (2.8%) < BTO–P (7.8%) < BTO–S (12.0%), respectively (Figure 5A). In case of ibuprofen lower activity was detected while the residential concentration follows the same order: BTO–R (7%) < BTO–P (26%) < BTO–S (42%), respectively (Figure 5C). To better evaluate photocatalytic activities of BTO samples, the reaction kinetics were analyzed as the first order reaction, and degradations were calculated from the slope of the corresponding linear plots (Figures 5B,D) using the Eq. 5 (Ohtani, 2013):

$$\ln(C_o/C) = kt \quad (5)$$

It can be seen from the fitted results in Figures 5B,D that the regression coefficient (R^2) values are close to unity indicating that the first-order decay kinetics (corresponding R^2 values are 0.986–0.970 for tetracycline, and 0.960–0.998 for ibuprofen) adequately explains the experimental results.

The estimated first-order rate constants are shown in Figure 6A for tetracycline and ibuprofen degradation. BTO–R displays the highest rate constant among all studied samples, suggesting that the nanorod morphology is beneficial for the pollutant degradation process. The kinetics of photocatalytic reactions at constant irradiance are described by a Langmuir–Hinshelwood-type rate law. However, the photocatalytic performance is determined by the amount of the adsorbed molecules. Therefore, for a meaningful

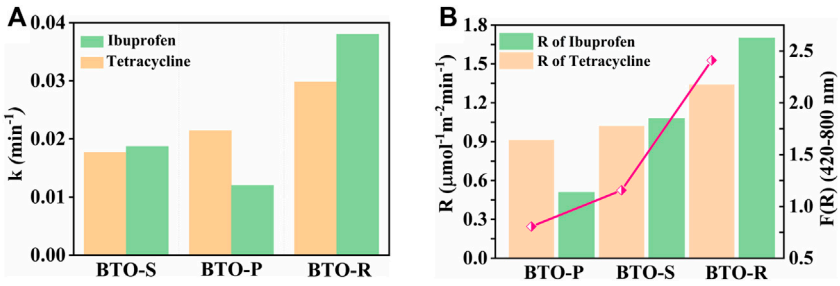

FIGURE 6
(A) Comparative first-order reaction constant and **(B)** apparent degradation rate of tetracycline (yellow bars) and ibuprofen (green bars) decompositions over as-synthesized BTO photocatalysts. **(B)** (Pink line with circles) F(R) values obtained through the integration in the wavelength range 420–800 nm.

comparison of the photocatalytic activities of phototocatalyst exhibiting the same crystallographic phase the reaction rates per unit surface area must be considered. Accordingly, the degradation performances for pollutant treatment were further analyzed by comparing the rates upon consideration of the surface area using Eq. 6 (Atitar et al., 2019):

$$R = \frac{V \cdot k \cdot C}{S_{BET} \cdot M_{cat.}} \quad (6)$$

where R is the degradation rate, V is the volume of the suspension, k first-order rate constant, C is pollutant concentration, S_{BET} is BET surface area of the photocatalysts, $M_{[cat.]}$ is the weight of the photocatalyst powder in the suspension. For both tetracycline and ibuprofen photocatalytic removal the apparent degradation rate increases in the order BTO–P (0.910 μmol m^{-2} min^{-1} and 0.511 μmol m^{-2} min^{-1}) < BTO–S (1.02 μmol m^{-2} min^{-1} and 1.079 μmol m^{-2} min^{-1}) < BTO–R (1.33 μmol m^{-2} min^{-1} and 1.702 μmol m^{-2} min^{-1}), respectively (Figure 6B). The nanorod shaped BTO still demonstrates the highest activity for the tetracycline and ibuprofen degradation.

The obtained dependence of the photocatalytic performance on the morphology of the BTO can arise from the different abilities of BTO samples to absorb the visible light. As Figure 6B shows the degradation rate increases as the F(R) in the visible wavelength range increases. According to the made observation, it can be concluded that the superior performance of the BTO-R upon illumination with visible light arises from its better ability to harvest visible light. Furthermore, better charge-carrier separation in BTO-R sample might be responsible for the obtained high performance. The corresponding results will be the focus of the next publication.

As the BTO-R demonstrated the highest photocatalytic activity, its recyclability was further investigated. Figure 7 shows unchangeable decomposition activity of BTO-R even after five cycles of treatment under visible light illumination.

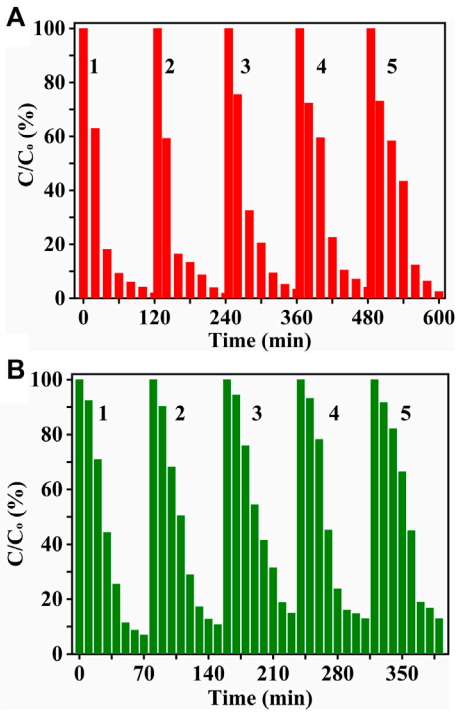

FIGURE 7
Repeated cycles up to 5 times for photocatalytic degradation of **(A)** tetracycline and **(B)** ibuprofen over BTO–R photocatalyst, respectively.

The long-term photocatalytic activity of BTO-R underlines its further advantages in pharmaceutical wastewater treatment.

To understand a wide range of environmental applications of BTO-R, the visible light degradation of Rhodamine B (RhB) and Methyl orange (MO) were investigated. Meanwhile, BTO-R does not only exhibit complete degradation of RhB and MO merely within 50 min of visible light illumination, but shows robust

character even after six cycles of photocatalytic degradation (Supplementary Figures S4, S5, in the SI). Upon visible light illumination, diverse pollutants can be deteriorated and gradually mineralized into small fragmentation e.g., CO_2, H_2O or inorganic ions NH_4^+, NH_3 etc (Hailili et al., 2017a). The evidence of mineralization was determined by the total organic carbon (TOC) analyses and exhibited 94.65, 83.82, 64.28 and 58.14% for the selected pollutants MO, RhB, tetracycline and ibuprofen, respectively (Supplementary Figure S6, in the SI). These results evince unselective degradation of diverse pollutants over BTO-R photocatalyst upon visible light illumination, implying their potential implementations in the field of environmental pollution control.

Mechanistic insights into the photocatalytic process

Generally, the advanced oxidation process involves photoexcitation of electrons from the valence band (VB) to the conduction band (CB); oxidation of organic compounds occurs either directly by the VB holes or indirectly *via* the surface bound hydroxyl radical ($^{\cdot}OH$) formed through the reaction of hydroxyl groups with the holes. The reaction of the electrons with O_2 can result in the formation of $O_2^{\cdot-}$ radicals. The production of species e.g., $O_2^{\cdot-}$ and $^{\cdot}OH$ is not only beneficial for the electron–hole separation by depletion of the e^- and h^+, but it promotes the degradation of the pollutants by their strong oxidation capability. Regarding BTO photocatalysts that acquire a similar crystal structure with $Bi_5FeTi_3O_{15}$, the superoxide radicals may play a certain role in the studied photocatalytic system (Hailili et al., 2017a). The radical quantification by an active species trapping method was conducted to determine the role of involved species in the tetracycline degradation. Herein, an inspection of active radicals was investigated by introducing ammonium oxalate (AO), isopropyl alcohol (IPA), p–benzoquinone (PBQ) and $K_2Cr_2O_7$ which act as h^+-,$^{\cdot}OH$-, e^-- and $O_2^{\cdot-}$-scavengers, respectively. When AO was added into the system as a hole scavenger, tetracycline degradation was inhibited and displayed 20.48% removal, suggesting that photoinduced h^+ was the prominent radical driving the tetracycline degradation; When $^{\cdot}OH$ scavenger, IPA, was introduced into the system, nearly 73.08% of tetracycline was degraded, indicating the limited role of $^{\cdot}OH$. However, when PBQ and $K_2Cr_2O_7$ agents were added to the reaction system, approximately 72.03 and 68.59% of antibiotics were retained in the solution, implying the dominant role of $O_2^{\cdot-}$ and e^- in the degradation process (Supplementary Figure S7A in SI). It is reasonable since the photoelectron-induced multistep reduction of surface adsorbed oxygen results in the generation of stronger oxidants such as $O_2^{\cdot-}$ radicals, promoting charge carrier separation and facilitating surface redox reactions. The ESR analyses of $^{\cdot}OH$ and $O_2^{\cdot-}$ trapping further validate the contributions of $O_2^{\cdot-}$ radicals to the pollutant degradation (Supplementary Figure S7B in SI). Hence, the simultaneous role of active species during the photocatalytic process, especially $O_2^{\cdot-}$ radicals promote charge carrier transport and together with strong oxidation capacities can decompose the tetracycline into small fragments (CO_2, H_2O and NH_3) until complete mineralization under visible light illumination occurs.

After active species in the photocatalytic reaction were identified we can summarize important parameters affecting the degradation mechanism of pollutants over BTO photocatalysts upon visible light illumination. The geometric structures and surface metrics are crucial factors for photocatalytic activity. The BTO includes TiO_6, TiO_5 and $Bi'O_6$ and $Bi''O_5$ polyhedra with different coordination modes. The roles of these units should be considered by the discussion of the efficiency, e.g., in the presence of TiO_6 with Ti–O–Ti connection the charger carrier transport is facilitated. In addition, investigations revealed that dipole moment and induced electronic field variations in semiconductors with distorted MO_6 octahedral promote charge carrier separation (Hailili et al., 2017b), and thus enhance the photocatalytic activities upon light illumination. Furthermore, the bond angle of Ti–O–Ti in BTO and the formed internal electric field between the $(Bi_2O_2)^{2+}$ and the $(Bi_2Ti_3O_{10})^{2-}$ layer enable charge carrier separation and improve the photocatalytic activity. Differently coordinated Bi–O polyhedral structures serve as electron donor sites to promote charge carrier separation in the layered structures, thus minimizing the waste of photoenergy through recombination reactions. Surface area is known also to influence photocatalytic performances. The determined surface areas of BTO are comparable, in which BTO–P and BTO–R possess similar areas (24.81 $m^2\,g^{-1}$ and 26.09 $m^2\,g^{-1}$). These results imply that identical amounts of molecules e.g., pollutants, O_2 and H_2O might be adsorbed on the surface of BTO samples. However, the BTO–R displays higher photocatalytic activity for pharmaceutical residues than BTO–P.

Hence, the higher activity of BTO-R in comparison to other BTO microstructures was assigned to the broader visible light absorption, promoting the more active species generation, resulting in an obvious enhancement in the further redox reactions. The observed shaped dependent variations in the light absorption might be caused by multiple reflections and scattering from assorted morphological BTO photocatalysts, resulting in significant decreases in the electronic band gaps. In addition, the directional growth and surface atomic arrangement-related shallow donor levels in the samples, especially in BTO-R, would greatly affect light scattering and reflection, resulting in strengthened light absorption. Further investigations are required to explain the light absorption of three BTO samples. In summary, the predominant photocatalytic

performance of shaped-controlled BTO results from effective charge carrier separations, dipole-induced built-in electronic field variations, surface areas, and broad visible light absorption.

Conclusion

A novel one-step ionic liquid mediated synthetic strategy was attempted for the microstructure regulations of layered perovskite $Bi_4Ti_3O_{12}$ (BTO) photocatalysts, which were utilized for environmental remediation. The following aspects are worth highlighting:

1) Morphology tailoring was achieved in hydrothermal synthesis merely by adjusting adding volumes of ionic liquid, 1-butyl-3-methylimidazolium iodide [Bmim]I. This preparation method contributed to the assorted morphology (spherical nanoparticles, nanoplates and nanorods), meanwhile resulting in high yields of BTO photocatalyst with band gap energies in the visible wavelength range (>2.9 eV). The formation mechanism of diverse morphologies and optical transitions were revealed based on the instinct structure of BTO controlled *via* ionic liquid. With the simplicity and universality of ionic liquid alteration, this method can be potentially extended for the microstructure controlled synthesis of further perovskite photocatalysts.
2) As-synthesized photocatalysts were investigated for the pollutant treatment by decomposing pharmaceutical residues and industrial contaminants. Results showed that BTO phoycatalysts served as an effective, robust and recyclable material and demonstrated high photocatalytic degradation rate of pharmaceutics. Herein, the nanorod shaped BTO showed superior performance in comparison to the spherical nanoparticles and nanoplates. A detailed analysis revealed the stronger visible light absorption of nanorods is responsible for its higher activity. Furthermore, nanorods exhibited enhanced performances for diverse pollutant treatments by decomposing methyl orange (99.8%), Rhodamine B (99.6%) and achieved 94.65% total organic carbon removal.
3) Radical scavenging and spin trapping tests confirmed the dominant role of such active species as h^+, e^-, and superoxide radicals for pollutant degradation. The high photoactivity of BTO photocatalysts was ascribed to the unique microstructures, visible light absorption and ability to form superoxide radicals. This simple preparation approach can pave the way for the purposive synthesis of other perovskite nanomaterials in microstructure regulation and will, in turn, motivate the practical applications of cost-effective, robust and highly efficient visible-light-driven photocatalysts in the field of environmental remediation.

Further studies are planned to enhance the visible photocatalytic activity of the BTO photocatalysts. This will involve the variation of the reaction conditions (temperature, time, pH, durations, molar ratios and variety of the ionic liquids), surface modification by introducing surface defects, exposed crystal facets, thickness, and active site regulations.

Data availability statement

The original contributions presented in the study are included in the article/Supplementary Material, further inquiries can be directed to the corresponding author.

Author contributions

All authors listed have made a substantial, direct, and intellectual contribution to the work and approved it for publication.

Funding

The authors are grateful to the National Natural Science Foundation of China (No. 21902161), the Alexander von Humboldt Foundation and the Postdoctoral Science Foundation of China (Nos. 2019T120137 and 2018M641484) for the financial funding.

Conflict of interest

The authors declare that the research was conducted in the absence of any commercial or financial relationships that could be construed as a potential conflict of interest.

Publisher's note

Supplementary material

The Supplementary Material for this article can be found online at: https://www.frontiersin.org/articles/10.3389/fctls.2022.890842/full#supplementary-material

References

Atitar, M., Ismail, A., Dillert, R., and Bahnemann, D. (2019). Photodegradation of herbicide imazapyr and phenol over mesoporous bicrystalline phases TiO_2: a kinetic study. *Catalysts* 9 (8), 640. doi:10.3390/catal9080640

Chen, C., Ma, W., and Zhao, J. (2010). Semiconductor-mediated photodegradation of pollutants under visible-light irradiation. *Chem. Soc. Rev.* 39, 4206. doi:10.1039/b921692h

Fujishima, A., and Honda, K. (1972). Electrochemical photolysis of water at A semiconductor electrode. *Nature* 238 (7), 37–38. doi:10.1038/238037a0

Gao, S., Gu, B., Jiao, X., Sun, Y., Zu, X., Yang, F., et al. (2017). Highly efficient and exceptionally durable CO_2 photoreduction to methanol over freestanding defective single-unit-cell bismuth vanadate layers. *J. Am. Chem. Soc.* 139 (9), 3438–3445. doi:10.1021/jacs.6b11263

Gong, H., Wang, L., Zhou, K., Zhang, D., Zhang, Y., Adamaki, V., et al. (2021). Improved photocatalytic performance of gradient reduced TiO_2 ceramics with aligned pore channels. *Adv. Powder Mater.* 1 (3), 100025. doi:10.1016/j.apmate.2021.11.011

Hailili, R., Wang, Z., Xu, M., Wang, Y., Gong, X., Xu, T., et al. (2017a). Layered nanostructured ferroelectric perovskite $Bi_5FeTi_3O_{15}$ for visible-light photodegradation of antibiotics. *J. Mater. Chem. A* 5 (40), 21275–21290. doi:10.1039/c7ta06618j

Hailili, R., Dong, G., Ma, Y., Jin, S., Wang, C., Xu, T., et al. (2017b). Layered perovskite $Pb_2Bi_4Ti_5O_{18}$ for excellent visible light-driven photocatalytic NO removal. *Ind. Eng. Chem. Res.* 56 (11), 2908–2916. doi:10.1021/acs.iecr.6b04706

Hailili, R., Wang, Z., Ji, H., Chen, C., Gong, X., Sheng, H., et al. (2022). Mechanistic insights into the photocatalytic reduction of nitric oxide to nitrogen on oxygen-deficient quasi-two-dimensional bismuth-based perovskites. *Environ. Sci. Nano* 9 (4), 1453–1465. doi:10.1039/D1EN01090E

Hoffmann, M., Martin, T., Choi, W., and Bahnemann, D. (1995). Environmental applications of semiconductor photocatalysis. *Chem. Rev.* 95 (1), 69–96. doi:10.1021/cr00033a004

Hou, J., Wang, Z., Yang, C., Zhou, W., Jiao, S., Zhu, H., et al. (2013). Hierarchically plasmonic Z-scheme photocatalyst of Ag/AgCl nanocrystals decorated mesoporous single crystalline metastable $Bi_{20}TiO_{32}$ nanosheets. *J. Phys. Chem. C* 117 (10), 5132–5141. doi:10.1021/jp311996r

Huddleston, J., Visser, A., Reichert, W., Willauer, H., Broker, G., Rogers, R., et al. (2001). Characterization and comparison of hydrophilic and hydrophobic room temperature ionic liquids incorporating the imidazolium cation. *Green Chem.* 3 (4), 156–164. doi:10.1039/b103275p

Keen, O., and Linden, K. (2013). Degradation of antibiotic activity during UV/H_2O_2 advanced oxidation and photolysis in wastewater effluent. *Environ. Sci. Technol.* 47 (22), 13020–13030. doi:10.1021/es402472x

Kubelka, P., and Munk, F. (1931). An article on Optics of paint layers. *Z. Technol. Phys.* 12, 593–601.

Li, R., Zhang, F., Wang, D., Yang, J., Li, M., Zhu, J., et al. (2013). Spatial separation of photogenerated electrons and holes among {010} and {110} crystal facets of $BiVO_4$. *Nat. Commun.* 4, 1432. doi:10.1038/ncomms2401

Liu, L., Huang, H., Chen, F., Yu, H., Tian, N., Zhang, Y., et al. (2020). Cooperation of oxygen vacancies and 2D ultrathin structure promoting CO_2 photoreduction performance of $Bi_4Ti_3O_{12}$. *Sci. Bull. (Beijing).* 65 (11), 934–943. doi:10.1016/j.scib.2020.02.019

Liu, H., Mei, H., Miao, N., Pan, L., Jin, Z., Zhu, G., et al. (2021). Synergistic photocatalytic NO removal of oxygen vacancies and metallic bismuth on $Bi_{12}TiO_{20}$ nanofibers under visible light irradiation. *Chem. Eng. J.* 414, 128748. doi:10.1016/j.cej.2021.128748

Lv, X., Lam, F. L. Y., and Hu, X. (2022). A review on bismuth oxyhalide (BiOX, X=Cl, Br, I) based photocatalysts for wastewater remediation. *Front. Catal.* 2, 839072. doi:10.3389/fctls.2022.839072

Minero, C., Maurino, V., and Vione, D. (2013). *Photocatalytic mechanisms and reaction pathways drawn from kinetic and probe molecules*. Weinheim, Germany: Wiley-VCH Verlag GmbH & Co. KGaA, 53–72. doi:10.1002/9783527645404

Nobbs, J. H. (1985). Kubelka-munk theory and the prediction of reflectance. *Rev. Prog. Coloration Relat. Top.* 15 (1), 66–75. doi:10.1111/j.1478-4408.1985.tb03737.x

Ohtani, D. (2013). *Design and development of active titania and related photocatalysts*, 73–102. doi:10.1002/9783527645404

Rappaport, S., and Smith, M. (2010). Environment and disease risks. *Science* 330 (6003), 460–461. doi:10.1126/science.1192603

Ren, J., Li, J., and Song, Z. (2016). Ionic liquid-assisted synthesis of $Bi_{12}TiO_{20}$ nanostructures and their visible-light photocatalytic performance. *Mater. Technol. (N. Y. N. Y).* 31 (10), 557–561. doi:10.1080/10667857.2016.1147129

Ren, F., Wang, J., Xie, F., Zan, K., Wang, S., Wang, S., et al. (2020). Applications of ionic liquids in starch chemistry: A review. *Green Chem.* 22 (7), 2162–2183. doi:10.1039/C9GC03738A

Schneider, J., Matsuoka, M., Takeuchi, M., Zhang, J., Horiuchi, Y., Anpo, M., et al. (2014). Understanding TiO_2 photocatalysis: Mechanisms and materials. *Chem. Rev.* 114 (19), 9919–9986. doi:10.1021/cr5001892

Tauc, J. (1968). Optical properties and electronic structure of amorphous Ge and Si. *Mater. Res. Bull.* 3 (1), 37–46. doi:10.1016/0025-5408(68)90023-8

Tong, H., Ouyang, S., Bi, Y., Umezawa, N., Oshikiri, M., Ye, J., et al. (2012). Nano-photocatalytic materials: Possibilities and challenges. *Adv. Mater.* 24 (2), 229–251. doi:10.1002/adma.201102752

Wang, Y., Deng, K., and Zhang, L. (2011). Visible light photocatalysis of BiOI and its photocatalytic activity enhancement by *in situ* ionic liquid modification. *J. Phys. Chem. C* 115 (29), 14300–14308. doi:10.1021/jp2042069

Wang, C., Chen, F., Hu, C., Ma, T., Zhang, Y., Huang, H., et al. (2022). Efficient piezocatalytic H_2O_2 production of atomic-level thickness $Bi_4Ti_3O_{12}$ nanosheets with surface oxygen vacancy. *Chem. Eng. J.* 431 (35), 133930. doi:10.1016/j.cej.2021.133930

Wei, Z., Zhao, Y., Jiang, J., Yan, W., Feng, Y., Ma, J., et al. (2020). Research progress on hybrid organic-inorganic perovskites for photo-applications. *Chin. Chem. Lett.* 31 (12), 3055–3064. doi:10.1016/j.cclet.2020.05.016

Wu, S., Xiong, J., Sun, J., Hood, Z., Zeng, W., Yang, Z., et al. (2017). Hydroxyl-dependent evolution of oxygen vacancies enables the regeneration of BiOCl photocatalyst. *ACS Appl. Mater. Interfaces* 9 (19), 16620–16626. doi:10.1021/acsami.7b01701

Yao, W., Wang, H., Xu, X., Shang, S., Hou, Y., Zhang, Y., et al. (2003). Photocatalytic property of perovskite bismuth titanate $Bi_4Ti_3O_{12}$. *Mater. Lett.* 57 (13), 1899–1902. doi:10.1016/S0167-577X(02)01097-2

Yao, W., Xu, X., Wang, H., Zhou, J., Yang, X., Zhang, Y., et al. (2004). Photocatalytic property of perovskite bismuth titanate. *Appl. Catal. B Environ.* 52 (2), 109–116. doi:10.1016/S0926-3373(04)00251-6

Zhang, H., Lü, M., Liu, S., Wang, L., Xiu, Z., Zhou, Y., et al. (2009). Preparation and photocatalytic property of perovskite $Bi_4Ti_3O_{12}$ films. *Mater. Chem. Phys.* 114 (2–3), 716–721. doi:10.1016/j.matchemphys.2008.10.052

Zhang, Y., Liu, W., Chen, S., Gao, Q., Li, Q., Zhu, X., et al. (2020). Ionic liquids for the controllable preparation of functional TiO_2 nanostructures: A review. *Ionics* 26, 5853–5877. doi:10.1007/s11581-020-03719-x

Zhang, X., Han, D., Chen, X., Chen, Y., Chang, S., Zhong, H., et al. (2021). Effects of solvent coordination on perovskite crystallization. *Acta Phys. -Chim. Sin.* 37 (4), 2008055. doi:10.3866/PKU.WHXB202008055

Zhao, X., Jin, W., Cai, J., Ye, J., Li, Z., Ma, Y., et al. (2011). Shape- and size-controlled synthesis of uniform anatase TiO_2 nanocuboids enclosed by active {100} and {001} facets. *Adv. Funct. Mater.* 21 (18), 3554–3563. doi:10.1002/adfm.201100629

Zhu, X., Zhang, J., and Chen, F. (2011). Study on visible light photocatalytic activity and mechanism of spherical $Bi_{12}TiO_{20}$ nanoparticles prepared by low-power hydrothermal method. *Appl. Catal. B Environ.* 102 (1–2), 316–322. doi:10.1016/j.apcatb.2010.12.019

Zong, X., Yan, H., Wu, G., Ma, G., Wen, F., Wang, L., et al. (2008). Enhancement of photocatalytic H_2 evolution on CdS by loading MoS_2 as cocatalyst under visible light irradiation. *J. Am. Chem. Soc.* 130 (23), 7176–7177. doi:10.1021/ja8007825